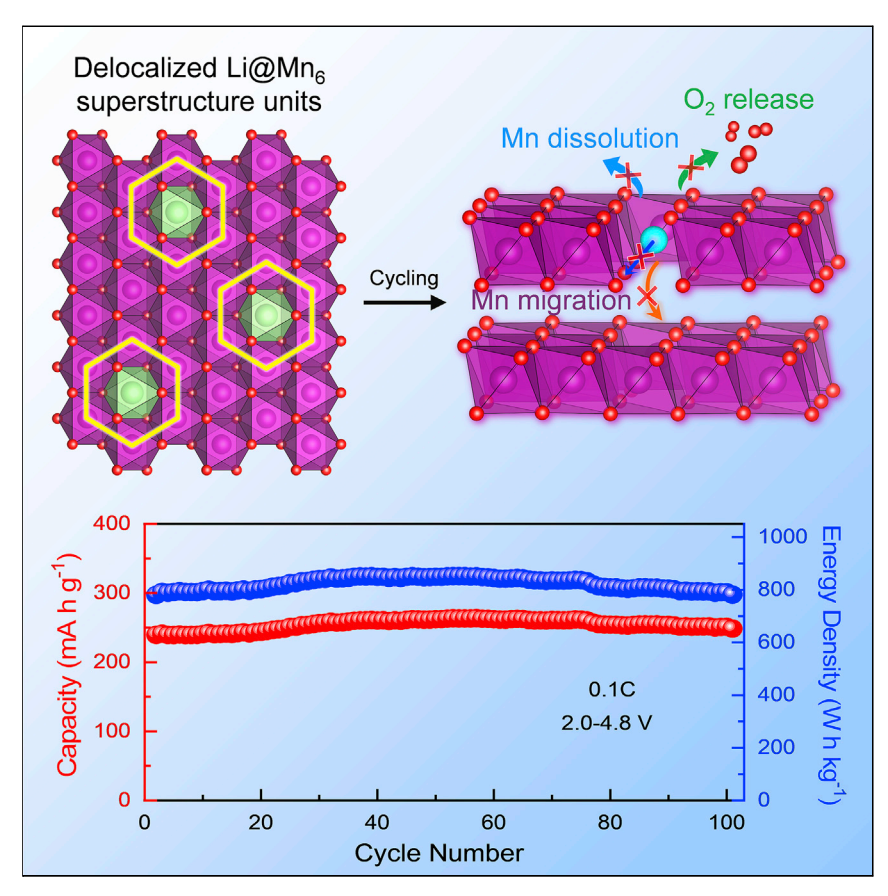
Chem



### **Article**

# Delocalized Li@Mn<sub>6</sub> superstructure units enable layer stability of high-performance Mn-rich cathode materials



Application of Li-excess Mn-rich layered oxide (LMRO) cathode is subject to severe structural instability. Herein, delocalization of the Li@Mn $_6$  superstructure units is proposed to realize stable LMRO. Various structural issues, such as intralayer/interlayer Mn migration, Mn dissolution, and O $_2$  release from anionic redox, have been effectively suppressed, which leads to stable electrochemical performance. This structural modification strategy provides guidance to achieve high-performance layered cathode materials.

Weiyuan Huang, Cong Lin, Jimin Qiu, ..., Xiaoyuan Li, Mingjian Zhang, Feng Pan

lincong@pku.edu.cn (C.L.) panfeng@pkusz.edu.cn (F.P.)

#### Highlights

Delocalizing Li@Mn<sub>6</sub> superstructure units is proposed to achieve a stable LMRO cathode

Various instability issues are inhibited leading to stable performance

Such a modification strategy opens up new research ideas for layered cathodes

Huang et al., Chem 8, 2163–2178 August 11, 2022 © 2022 Elsevier Inc. https://doi.org/10.1016/j.chempr.2022.04.012





## Chem



#### **Article**

# Delocalized Li@Mn<sub>6</sub> superstructure units enable layer stability of high-performance Mn-rich cathode materials

Weiyuan Huang,<sup>1</sup> Cong Lin,<sup>1,\*</sup> Jimin Qiu,<sup>1</sup> Shunning Li,<sup>1</sup> Zhefeng Chen,<sup>1</sup> Haibiao Chen,<sup>2</sup> Wenguang Zhao,<sup>1</sup> Guoxi Ren,<sup>3</sup> Xiaoyuan Li,<sup>1</sup> Mingjian Zhang,<sup>1</sup> and Feng Pan<sup>1,4,\*</sup>

#### **SUMMARY**

The search for cathode materials with high energy density, longterm cycling stability, and low cost is one of the most important challenges for current lithium-ion batteries. To address the structural instability in Mn-rich layered cathodes, we demonstrate herein through thorough experimental and theoretical studies that delocalizing Li@Mn6 superstructure units within transition-metal layers is an effective strategy to enhance the layer stability of a Li-excess Mn-rich layered oxide (LMRO) cathode. The delocalized Li@Mn<sub>6</sub> superstructure units can not only increase the Mn valence to inhibit the adverse Jahn-Teller effect but also harness the anionic redox activity with suppressed O-Mn<sub>0</sub> species. Benefited from its stable layered structure, the LMRO cathode can retain a high capacity and energy density of 251 mA h g<sup>-1</sup> and 791 W h kg<sup>-1</sup>, respectively, after 100 cycles with nearly 100% retention. This work provides a feasible route to develop the high-performance layered cathodes with stable anionic redox chemistry.

#### INTRODUCTION

The burgeoning market of the grid-scale energy storage systems and electric vehicles has been rapidly expanding in recent years and demanding novel cathode materials with the strengths of high energy density, long-term cycling stability, and low cost. <sup>1–3</sup> The widespread layered oxide cathodes in today's commercial lithium-ion batteries (LIBs) are either LiCoO<sub>2</sub> (LCO) or Ni-rich Li[Ni $_x$ Co $_y$ (Al or Mn)<sub>1-x-y</sub>]O<sub>2</sub> (NCA or NCM, respectively), but unfortunately, these materials both suffer from the high cost of the Co due to its limited reserve, insufficient capacity, and poor cyclic stability. <sup>4–8</sup> To address the cost issue, the Co-less cathode systems are being widely explored recently. <sup>9,10</sup> Among the alternative transition metals (TMs), Mn is by far the most attractive, since it is not only remarkably cheaper than Co at a tenth of the cost but also free of toxicity, <sup>11,12</sup> and hence, the Mn-rich layered oxides have aroused great research interest.

Two representative Mn-rich layered oxide cathodes have been explored. One is the stoichiometric layered LiMnO $_2$  with a structure similar to the aforementioned LCO, NCA, or NCM but is thermodynamically unstable and rather difficult to directly synthesize. <sup>13,14</sup> The edge-sharing MnO $_6$  octahedra in the TM layers of LiMnO $_2$  are highly unstable because of the Jahn-Teller (J-T) distortion from the Mn $^{3+}$  ions, leading to the adverse structural transformation upon electrochemical cycling. For instance, Bruce's group reported a LiMnO $_2$  prepared by ion exchange from the layered NaMnO $_2$  precursor offering a high initial capacity of  $\sim$ 200 mA h g $^{-1}$ . <sup>15</sup> However,

#### THE BIGGER PICTURE

Cost-effective and non-toxic Liexcess Mn-rich layered oxide (LMRO) is one of the most promising cathodes for nextgeneration lithium-ion batteries, but unfortunately, it suffers from severe structural instability. Herein, we propose and validate the delocalization of the Li@Mn<sub>6</sub> superstructure units within the transition-metal (TM) layers as a structural modification strategy to achieve a stable LMRO cathode. Owing to such a structural feature, various issues such as intralayer/ interlayer Mn migration, Mn dissolution, and, more importantly, the anionic redox activity and irreversible phase transition have all been effectively inhibited. This leads to higher electrochemical performance than that of commercial Ni- and Co-based cathodes. This work reveals the significance of local structure and also suggests an approach to improve the LMRO stability, providing ideas for the future development of layered cathodes.







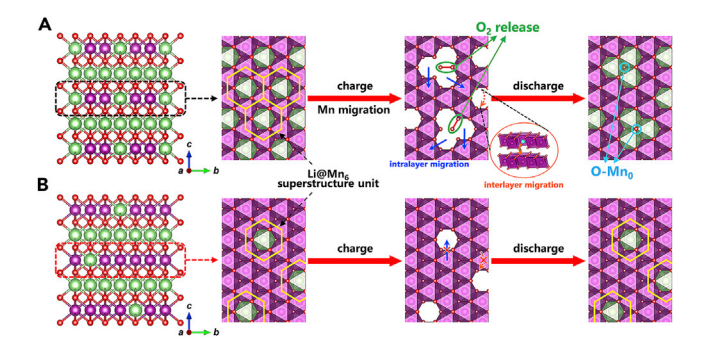


Figure 1. Impact of Li@Mn<sub>6</sub> superstructure units on layer stability

(A) Layered structure evolution of  ${\rm Li_2MnO_3}$  with localized  ${\rm Li@Mn_6}$  superstructure units during cycling.

(B) Layered structure evolution of LMRO with delocalized  $Li@Mn_6$  superstructure units during cycling.

the J-T distortion of the  $\rm Mn^{3+}O_6$  octahedra triggered an undesirable transition from the layered structure to the spinel phase upon cycling, resulting in the fast capacity decay. Therefore, the stoichiometric  $\rm LiMnO_2$  does not seem to be a promising cathode for LIBs.

Another option is the Li-excess  $Li_{1+x}Mn_{1-x-y}M_yO_2$  (M = Ni, Co) material, such as  $Li_2MnO_3$ ,  $Li_{1.2}Mn_{0.54}Ni_{0.13}Co_{0.13}O_2$ , and  $Li_{1.2}Mn_{0.6}Ni_{0.2}O_2$ , where the excess  $Li_{1.2}Mn_{0.54}Ni_{0.13}Co_{0.13}O_2$ ions are locally confined within the TM layers in form of the Li@Mn6 superstructure units (yellow hexagons in Figures 1 and \$1A), i.e., one LiO<sub>6</sub> octahedron encircled by six MnO<sub>6</sub> octahedra arranging in a hexagonal pattern. Such superstructure units, in terms of structure, can induce the so-called superlattice peaks in the 20°-30° range of powder X-ray diffraction (XRD) that are subject to the actual stacking faults and the degree of Li/Mn ordering with the Li concentration in the TM layers (Figure S1B), making them commonly convoluted into asymmetric broad peaks with low intensity in real XRD patterns (Figures S1C-S1E). 16-20 In these Li-excess Mn-rich layered cathodes, extra capacity can be unleashed by the anionic redox of the O in addition to the Mn redox (Figure 1A). <sup>21–23</sup> Despite the presence of excess Li, which can raise the initial Mn oxidation state to +4 to circumvent the J-T effect, <sup>24–27</sup> these O3-type layered compounds nonetheless undergo structural evolution during the electrochemical process. Specifically, in these Li-excess layered oxides, the coordination environment around the O atom is typically set by two Li-O-Mn and one Li-O-Li configurations (Mn<sub>2</sub>Li-O-Li<sub>3</sub>). Unfortunately, the unhybridized O 2p state in the Li-O-Li link is more easily oxidized during charging than the hybridized counterpart due to its higher energy and will thus lead to the uncontrollable anionic redox activity. <sup>28</sup> As shown explicitly in Figure 1A, Li ions in the TM layers are extracted upon charging, causing the formation of abundant vacancies that facilitate the Mn-ion migration both into the Li slabs (interlayer migration) and within the TM layers (intralayer migration). Migration of the Mn ions results in not only the irreversible transition to the spinel-like phase and the destruction of the Li@Mn<sub>6</sub> superstructure units but also more seriously the formation of the O-Mn<sub>0</sub> species within the larger vacancies after rearrangement. As a result, gaseous O loss from the structure and, further, the structural degradation will take place during the long-term cycling.<sup>29,30</sup> Xia's group reported an O3-type layered cathode,  $Li_{0.700}[Li_{0.222}Mn_{0.756}]O_2$ , whose Li and Mn within the TM layers are disorderly arranged because of the absence of the superlattice peaks in its XRD pattern (Figure S1F).<sup>31</sup> This Li/Mn disordering modulates the O redox activity and the Li-ion extraction behavior, which improves the structural stability with mitigated J-T

<sup>&</sup>lt;sup>1</sup>School of Advanced Materials, Peking University Shenzhen Graduate School, Shenzhen 518055, People's Republic of China

<sup>&</sup>lt;sup>2</sup>Institute of Marine Biomedicine, Shenzhen Polytechnic, Shenzhen 518055, People's Republic of China

<sup>&</sup>lt;sup>3</sup>State Key Laboratory of Functional Materials for Informatics, Shanghai Institute of Microsystem and Information Technology, Chinese Academy of Sciences, Shanghai 200050, China

<sup>&</sup>lt;sup>4</sup>Lead contact

<sup>\*</sup>Correspondence: lincong@pku.edu.cn (C.L.), panfeng@pkusz.edu.cn (F.P.)

https://doi.org/10.1016/j.chempr.2022.04.012





distortion and leads to the enhanced electrochemical cycling performance ( $\sim$ 80% capacity retention after 100 cycles at 1C [1C = 250 mA g<sup>-1</sup>]). Previous studies have shown that the O2-type layered structure can inhibit the irreversible Mn migration during cycling, thus improving the cyclic stability to some extent. However, these reported O2-type Mn-rich layered cathodes still have unsatisfactory cyclic stability after the long-term cycles, with the capacity retention such as  $\sim$ 74% after 40 cycles at C/50 for the Li<sub>0.83</sub>[Li<sub>0.2</sub>Ni<sub>0.2</sub>Mn<sub>0.6</sub>]O<sub>2</sub><sup>32</sup> and  $\sim$ 66% after 50 cycles at C/20 for the Li<sub>1.25-y</sub>Mn<sub>0.5</sub>Co<sub>0.25</sub>O<sub>2</sub>. <sup>33</sup> Thus, there are still challenges to design the Liexcess Mn-rich layered oxides (LMROs) with suppressed irreversible phase transition along with O<sub>2</sub> release, Mn dissolution, and the resultant continuous voltage and capacity deterioration after the long-term cycling, which seriously impedes their practical applicability. <sup>34–36</sup>

Based on the origin of the structural instability mentioned above, one could identify that the TM–O layer stability related to the Li@Mn<sub>6</sub> superstructure units is the key toward the structural and electrochemical stability of the LMROs. Recently, Cho's group demonstrated that the excess-Li segregation forming the edge-sharing Li@Mn<sub>6</sub> superstructure units, like in Li<sub>2</sub>MnO<sub>3</sub>, would, unfortunately, trigger the electrochemical irreversibility due to the reduced Mn–O covalency and excessive O oxidation upon cycling. <sup>37,38</sup> Therefore, dispersing the Li@Mn<sub>6</sub> superstructure units within the TM layers is proposed as a feasible strategy to stabilize both the structure and electrochemistry of the Li-excess Mn-rich layered cathodes, which is different from the Li/Mn disordering scenario reported by Xia et al. <sup>31</sup> As illustrated in Figure 1B, despite the reduced Li content within the TM layers, the delocalized Li@Mn<sub>6</sub> superstructure units dispersedly arranged in the LMROs are expected to ensure a more reversible and stable structure since both the interlayer and intralayer Mn migration and the O loss during cycling can be significantly suppressed due to the spatial separation of the charge-induced vacancies.

By subtly introducing the Li@Mn<sub>6</sub> superstructure units into the LiMnO<sub>2</sub> host to mitigate the J-T distortion from the  $\mathrm{Mn^{3+}O_{6}}$  octahedra and to stabilize the lattice Mn and O, we herein report an O3-type LMRO, Li<sub>0.78</sub>Mn<sub>0.85</sub>Ni<sub>0.04</sub>O<sub>2</sub>, with delocalized Li@Mn<sub>6</sub> superstructure units within the TM layers and pristine Li deficiency in the alkali metal (AM) layers. This cathode material exhibits the stable Li@Mn<sub>6</sub> superstructure units that can be surprisingly retained without Mn dissolution even after the long-term cycling, and the anionic redox activity is thus inhibited with effectively suppressed O<sub>2</sub> release. Hence, originating from the enhanced layer stability, the LMRO cathode delivers a high capacity of 251 mA h  $g^{-1}$  with the corresponding energy density of 791 W h kg<sup>-1</sup> and almost 100% retention even after 100 cycles in the voltage window of 2.0-4.8 V. Further widening the voltage range to 1.5-4.8 V, an ultrahigh capacity of 329 mA h g<sup>-1</sup> and an energy density of 937 W h kg<sup>-1</sup> with over 88% retention after 100 cycles can also be achieved. Our work successfully demonstrates that delocalization of the Li@Mn<sub>6</sub> superstructure units should be a feasible strategy in suppressing the adverse J-T effect of the Mn<sup>3+</sup>O<sub>6</sub> octahedra and stabilizing the lattice Mn and O in the Mn-rich layered cathodes for realizing high-performance LIBs.

#### **RESULTS**

#### Structure characterization

The LMRO cathode material was prepared by an ion-exchange method from the P3-type layered sodic precursor (see supplemental information; Figure S2). Scanning electron microscopy (SEM) reveals that the LMRO product contains the



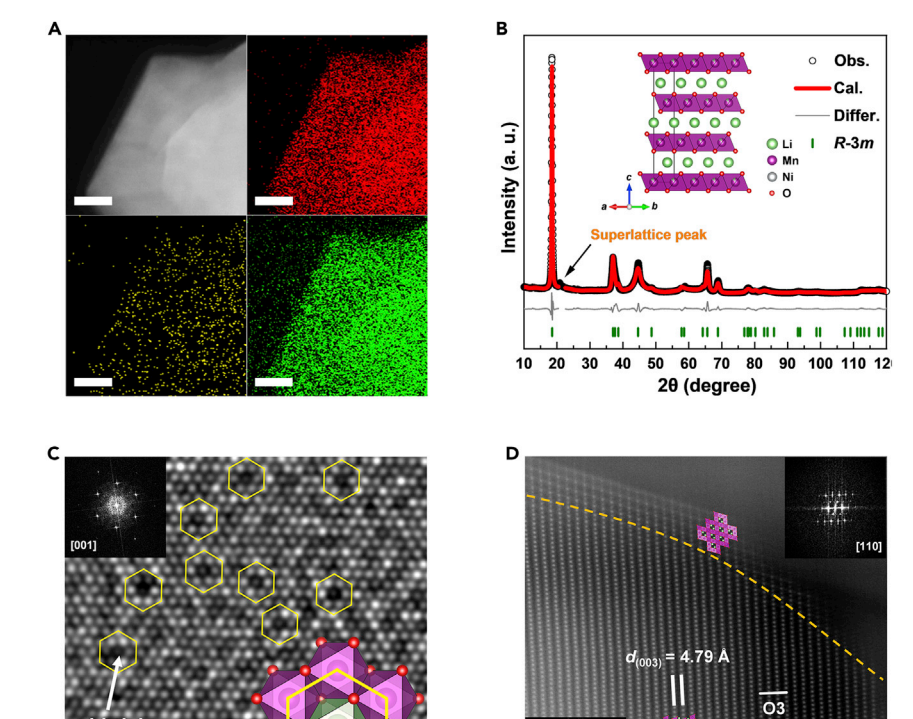


Figure 2. Structural characterization of LMRO

(A) STEM image and corresponding EDS mapping of Mn (red), Ni (yellow), and O (green). Scale bars, 20 nm.

(B) Rietveld XRD refinement (inset showing the layered oxide structure along the [110] direction). (C) HAADF-STEM image along the [001] zone axis (insets showing the corresponding FFT pattern and Li@Mn $_6$  superstructure units highlighted by the yellow hexagons). Scale bars, 1 nm.

(D) HAADF-STEM image along the [100] zone axis (insets showing the corresponding FFT patterns and structures). Scale bars, 2 nm.

spherical particles of 1–2 μm comprising nanoscale primary particles (Figure S3). Energy-dispersive X-ray spectroscopy (EDS) mapping clearly validates that the compositional Mn, O, and minor Ni elements are uniformly distributed throughout the particles (Figure 2A). Quantitative elemental composition of LMRO was analyzed by the inductively coupled plasma-atomic emission spectroscopy (ICP-AES, Table S1), and the obtained chemical formula of Li<sub>0.78</sub>Mn<sub>0.85</sub>Ni<sub>0.04</sub>O<sub>2</sub> confirms the Mn-rich and Lideficient nature. To explore the intrinsic structure, Rietveld refinement against the XRD pattern of LMRO was conducted, and it reveals the typical layered oxide framework with the R-3m space group (Figure 2B; Tables S2 and S3). Noticeably, in the LMRO formula, there is only 0.11 Li<sup>+</sup> in the TM layer (3a site) and 0.67 Li<sup>+</sup> in the AM layer (3b site). In addition, an unindexed peak at  $\sim$ 20.8° is also observed and identified as the superlattice peak, which specifies the presence of the Li/Mn ordering, i.e., the Li@Mn<sub>6</sub> superstructure units, in the TM layers and indicates the fundamental difference in structure between LMRO and previous reported  $\text{Li}_{0.700}[\text{Li}_{0.222}\text{Mn}_{0.756}]\text{O}_2$  with disordered Li/Mn arrangement. <sup>31</sup> Additionally, the  $Li@Mn_6$  superstructure units are not affected by the Ni doping, as LMRO and its controls without and with more Ni dopant (Li<sub>0.78</sub>Mn<sub>0.89</sub>O<sub>2</sub> and Li<sub>0.78</sub>Mn<sub>0.85</sub>Ni<sub>0.08</sub>O<sub>2</sub>, denoted as LMRO-Ni<sub>0</sub> and LMRO-Ni<sub>0.08</sub>, respectively) all possess identical superlattice peaks (Figures 2B and S4A). To obtain more detailed LMRO structural information at





the atomic scale, high-angle annular dark-field scanning transmission electron microscopy (HAADF-STEM) was employed to enable the direct observation of both the intralayer and interlayer atomic arrangements. As shown from the [001] zone axis with several stacked TM-oxide layers in Figure 2C, due to the obvious contrast between Li and Mn, the Li@Mn<sub>6</sub> superstructure units can be visually identified and found to be distributed in the delocalized form rather than a localized one as existed in the Li<sub>2</sub>MnO<sub>3</sub> (Figure 1). The O3-type layered structure of LMRO is also visualized from the [100] zone axis with the interlayer spacing of  $\sim$ 4.79 Å that corresponds to the (003) lattice plane (Figure 2D), further confirming the results from XRD refinement. Besides, a spinel-like phase layer with a thickness of  $\sim$ 2 nm is discovered on the surface of the bulk layered phase, as confirmed by the fast Fourier transform (FFT) pattern (insets in Figure 2D). This might be induced by the minor Ni dopant because LMRO-Ni<sub>0</sub> without Ni doping does not exhibit such surface spinel-like phase, whereas LMRO and LMRO-Ni<sub>0.08</sub> do (Figures 2D, S4B, and S4C). Overall, LMRO possesses the typical layered oxide structure with delocalized Li@Mn<sub>6</sub> superstructure units, which are thought to cast a meaningful impact on both the structural and electrochemical stabilities.

#### **Electrochemical performance**

The electrochemical performance of the LMRO cathode was evaluated by assembling the 2032-type coin cell with Li metal as the anode (see supplemental information). The voltage-capacity profiles for the initial two cycles in the voltage range of 2.0–4.8 V at 0.1C (1C = 250 mA  $g^{-1}$ ) are displayed in Figure 3A. Although LMRO only delivers a capacity of  $\sim$ 170 mA h g<sup>-1</sup> in the 1<sup>st</sup> charge, a much higher capacity of over 250 mA h g<sup>-1</sup> is achieved in the subsequent discharge process. A prelithiation treatment, i.e., firstly discharging to 2.0 V, was also conducted, and it leads to a much higher charge capacity of  $\sim$ 275 mA h g<sup>-1</sup> together with a high Columbic efficiency (CE) of  $\sim$ 90% in the 1<sup>st</sup> cycle (Figure S5A). Combining these results, it is readily to note that the extra charge capacity is mainly derived from the voltage below 3.3 V but not the plateau above 4.5 V, further confirming the Li-deficient feature of LMRO with vacancies in the AM layers and in consistency with the synthesis recipe and ICP-AES formula. Previously reported Li-rich manganese layered oxides, for instance,  $Li_{0.700}[Li_{0.222}Mn_{0.756}]O_2$  and  $Li_{1.20}Mn_{0.56}Co_{0.16}Ni_{0.08}O_2$ , usually exhibit a 1<sup>st</sup>-charge capacity of  $\sim$ 200 mA h g $^{-1}$  with a prolonged voltage plateau above 4.5 V, which is attributed to the oxidation of the lattice oxygen from  $O^{2-}$  to the  $O^{-}/O_2^{2-}$  or  $O_2$ gas. 31,39,40 In sharp contrast, the plateau above 4.5 V in the LMRO charge curve is much shorter than that reported by Xia et al. to contribute less than 100 mA h  $g^{-1}$ capacity (Figures 3A and S5A), suggesting the limited anionic redox activity. When compared with the commercial LCO and NCM811 (LiNi<sub>0.8</sub>Co<sub>0.1</sub>Mn<sub>0.1</sub>O<sub>2</sub>) cathodes cycled in the common voltage range of 3.0-4.5 and 2.7-4.3 V at 0.1C, respectively, LMRO provides an energy density of 807 W h  $kg^{-1}$  that is larger than these two opponents (Figure 3B). To unravel the electrochemical behaviors of the LMRO cathode during the charge/discharge process, cyclic voltammetry (CV) with the scan rate of 0.1 mV s<sup>-1</sup> was employed, and the result is shown in Figure S5B. The oxidation peak at  $\sim$ 4.7 V in the 1 $^{\rm st}$  positive scan can be assigned to the activation process (marked by the orange arrow in Figure S5B), 41,42 which becomes weaker in the following cycles, whereas the strongest peaks occur near 3 V, corresponding to the Mn<sup>3+</sup>/Mn<sup>4+</sup> redox pair. In summary, these results indicate that the high capacity of LMRO is related to the Mn<sup>3+</sup>/Mn<sup>4+</sup> redox reaction with limited anionic redox activity.

Detailed electrochemical characterization demonstrates that the LMRO cathode possesses the remarkable specific capacity, energy density, and cycling stability.





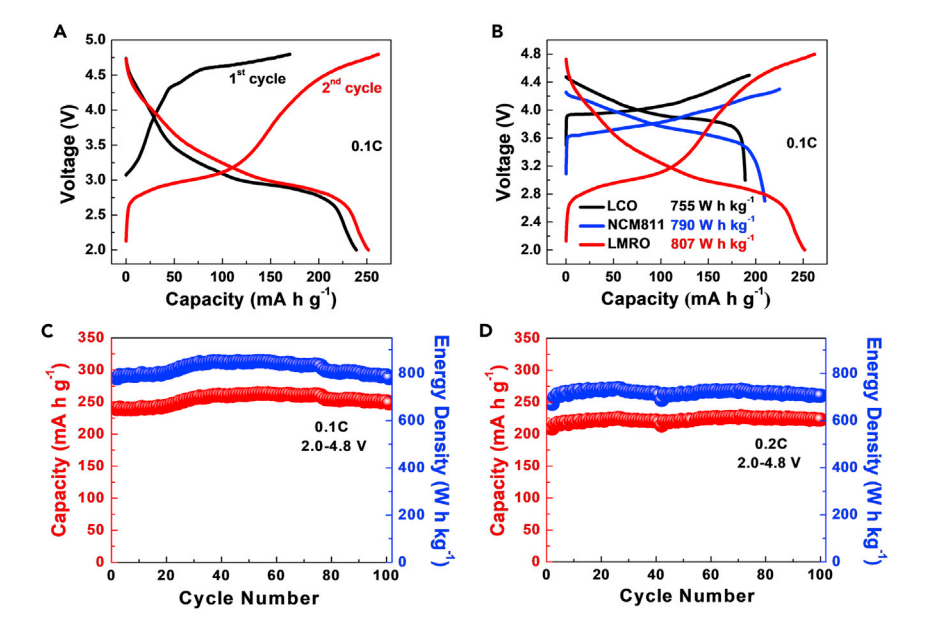


Figure 3. Electrochemical performance of LMRO (A) Voltage-capacity profiles for the initial two cycles in the voltage range of 2.0-4.8 V at 0.1C. (B) Comparison of the voltage-capacity profiles at 0.1C between LCO, NCM811, and LMRO.

(C) Long-term cycling capacity and energy density as cycled in the voltage range of 2.0-4.8 V

(D) Long-term cycling capacity and energy density as cycled in the voltage range of 2.0-4.8 V at 0.2C.

The rate performance of the LMRO cathode was firstly evaluated from 0.1C to 20C in the voltage range of 2.0-4.8 V. As shown in Figure S5C, a high capacity of  $\sim$ 250 mA h g<sup>-1</sup> is measured at 0.1C and retained after the test, whereas the capacity values at the specific 0.5C, 1C, and 2C are 187, 163, and 132 mA h  $g^{-1}$ , respectively. As regards the long-term cycling performance, when cycled in the voltage range of 2.0-4.8 V at 0.1 C, LMRO delivers a reversible capacity of 241 mA h g<sup>-1</sup> (corresponding to the energy density of 792 W h kg<sup>-1</sup>) and retains a rather high capacity of 251 mA h g<sup>-1</sup> (corresponding to the energy density of 791 W h kg<sup>-1</sup>) even after 100 cycles (Figure 3C), along with a small drop in the average discharge voltage of  $\sim$ 0.11 V (corresponding to  $\sim$ 0.0011 V per cycle) (Figures S5D–S5F). The slight capacity increase indicates a slow but continuous activation process during cycling. The diffusion coefficients of LMRO when cycled in the voltage range of 2.0-4.8 V at 0.1C were determined from the discharge branch of the galvanostatic intermittent titration technique (GITT) data (Figure S6), and their values are mostly close to  $10^{-12}$  cm<sup>2</sup> s<sup>-1</sup>. Further increasing the rate to 0.2C, an initial capacity of 215 mA h  $\rm g^{-1}$  (corresponding to the energy density of 700 W h  $\rm kg^{-1}$ ) and an even higher capacity of 223~mA h  $\text{g}^{-1}$  (corresponding to the energy density of 707 W h kg<sup>-1</sup>) after 100 cycles can also be provided by LMRO (Figure 3D), which only starts to decay after  $\sim$ 130 cycles and reaches the decent  $\sim$ 180 mA h g<sup>-1</sup> capacity (corresponding to the capacity retention of 83.7% and an energy density of 541 W h kg<sup>-1</sup>) after 200 cycles with the total drop in the average discharge voltage of  $\sim$ 0.19 V (corresponding to  $\sim$ 0.00095 V per cycle) (Figure S7).  $^{22,32,33,42,43}$  Moreover, it is remarkable that at 0.1C and 0.2C, there is virtually no decay in capacity or average voltage after 100 cycles. In order to further verify its potential use in practical batteries, the LMRO cathode was assembled into full cells using lithiated SiO<sub>x</sub> as the anode (see supplemental information). As shown in Figure S8, when cycled in the





voltage range of 1.8–4.7 V at 0.2C, two full cells employing the LMRO cathode both show decent cyclic stability with nearly 100% retention after long-term cycling, delivering high capacities of  $\sim\!222$  and  $\sim\!227$  mA h g $^{-1}$  after 120 and 70 cycles, respectively. When the voltage window is broadened to 1.5–4.8 V, a new discharge plateau appears at  $\sim\!1.7$  V in the LMRO discharge, which is ascribed to the extra Li<sup>+</sup> inserting into the tetragonal sites within the Li slabs and contributes to the capacity of  $\sim\!95$  mA h g $^{-1}$  at 0.2C (Figure S9A).  $^{44,45}$  Consequently, an ultrahigh capacity of 329 mA h g $^{-1}$  (corresponding to the energy density of 937 W h kg $^{-1}$ ) is achieved impressively, which is even retained at 289 mA h g $^{-1}$  (corresponding to the energy density of 811 W h kg $^{-1}$ ) with a high capacity retention of 88% (energy density retention of 87%) after 100 cycles (Figure S9B). The superior cycling stability strongly implies the high structural stability of LMRO during the electrochemical process.

When comparing the electrochemical performance of LMRO with its controls, LMRO-Ni<sub>0</sub> allows a somewhat lower cycling capacity, whereas LMRO-Ni<sub>0.08</sub> delivers a substantially smaller one (Figure S10). This indicates that more Ni dopant is detrimental to capacity and LMRO exhibits the optimal electrochemical performance. For further comparison, another two representative Mn-rich layered cathodes, i.e., Li<sub>2</sub>MnO<sub>3</sub> and Li<sub>0.7</sub>MnO<sub>2</sub>, were also synthesized and characterized structurally and electrochemically (see supplemental information). As shown in Figures S11A and S11B, although the Li<sub>2</sub>MnO<sub>3</sub> and Li<sub>0.7</sub>MnO<sub>2</sub> products both possess the typical layered oxide structure as verified by their XRD patterns, their atomic arrangements in the TM layers are totally different from that of LMRO: localized Li@Mn6 superstructure units are implied by the strong superlattice peaks in Li<sub>2</sub>MnO<sub>3</sub> (marked by the red frame in Figure S11A), whereas the Li@Mn<sub>6</sub> superstructure units are completely absent in Li<sub>0.7</sub>MnO<sub>2</sub> as suggested by the lack of the superlattice peaks (marked by the red-dotted frame in Figure S11B) and the Li-deficient formula. The different structures are expected to bring diverse electrochemical performance. The capacity and energy density provided by these reference materials when cycled in the voltage range of 2.0-4.8 V at 0.2C are much lower and rapidly degraded accompanied with distinct voltage decay (Figures S11C-S11E). Besides the above Li<sub>2</sub>MnO<sub>3</sub> and Li<sub>0.7</sub>MnO<sub>2</sub> opponents, other Li-rich Mn-based layered cathodes previously investigated, such as  $Li_{1.2}Mn_{0.54}Ni_{0.13}Co_{0.13}O_2$ ,  $Li_{1.03}Mn_{0.6}Ni_{0.2}O_2$ , and  $Li_{1.080}Mn_{0.503}Ni_{0.387}Co_{0.030}O_2$ , all suffer from the severe deterioration in the electrochemical performance. 32,46–48 By sharp contrast, the LMRO cathode can retain both the high and stable capacity and energy density after the long-term cycling, much superior to most of the reported layered oxide cathodes likely owing to its inherently stable layered structure (Table S4). 32,47,48

#### Structure and chemical state evolution during cycling

To obtain a convincing correlation between the excellent electrochemical performance and the structure of LMRO, mechanism studies were then conducted in depth. *In-situ* synchrotron high-energy XRD (HEXRD) was firstly used to track the structural changes of the first two charge/discharge cycles in the voltage range of 2.0–4.8 V at 0.25C. The time-voltage profile and the evolution of three major peaks are shown in Figure 4A. All the peaks evolve smoothly and are in good agreement with the time-voltage profile. In a quantitative analysis, the cell parameters of LMRO are extracted to show their evolution as presented in Figure 4B. During the charge and discharge processes, the lengths of the a-axis and c-axis, as well as the cell volume (V), are all decreased and increased, with their changes estimated to be only 1.9% and 2.2%, respectively, thus implying a stable LMRO structure. As Li<sup>+</sup> is extracted from LMRO, oxidation of the O<sup>2-</sup> and TM species occurs and results in a decrease of both the electrostatic repulsion due to the



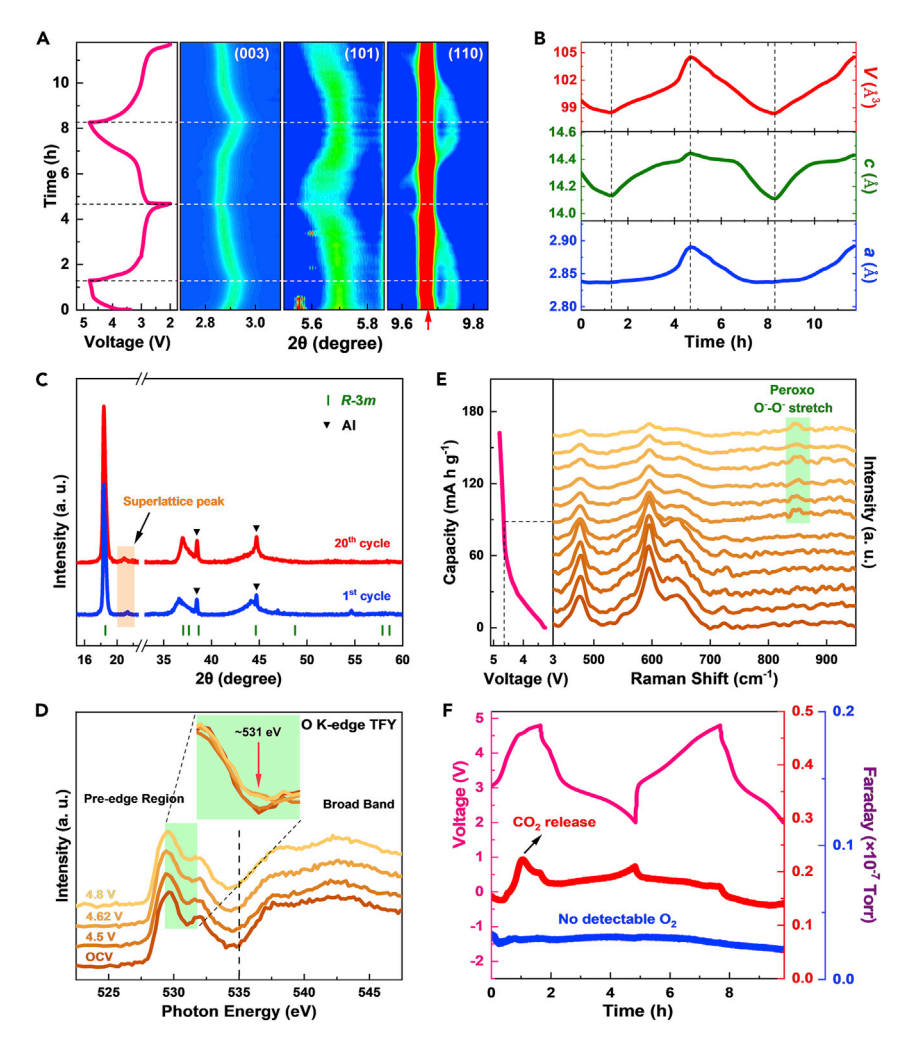


Figure 4. Structural and chemical state evolution of LMRO during cycling

(A) In-situ synchrotron HEXRD contour patterns showing three typical peaks with the corresponding time-voltage profiles for the initial two cycles in the voltage range of 2.0–4.8 V at 0.25C (red arrow indicating the strong signal from the Al current collector).

- (B) Extracted variations in a-axis and c-axis length and cell volume from (A).
- (C) Ex-situ XRD patterns after the 1st and 20th cycle in the voltage range of 2.0-4.8 V at 0.1C.
- (D) Ex-situ O K-edge XAS spectra collected in the TFY mode for the 1st charge to 4.8 V at 0.25C (inset showing the enlarged region of 529.5–532 eV).
- (E) In-situ Raman spectra for the 1st charge to 4.8 V at 0.12C.
- (F) In-situ DEMS curves for the initial two cycles in the voltage range of 2.0-4.8 V at 0.25C.

decreased charge density of the adjacent O layers and the TM–O bond length in the TM layers. As a result, the a-axis and c-axis of LMRO decrease while charging. Upon discharge, Li<sup>+</sup> inserts back into both the AM and the TM layers, and the a-axis and c-axis are thus expanded and completely recovered. Besides, during the charge/discharge process, no new Bragg peak appears, implying the high structural reversibility of LMRO. These results are also well backed up by the high-resolution transmission electron microscopy (HRTEM) and the HAADF-STEM of the LMRO at the 1<sup>st</sup> discharge state, clearly indicating the well-maintained O3-type layered structure with slightly increased interlayer spacing (Figures \$12A and \$12B) as well as the well-preserved delocalized Li@Mn<sub>6</sub> superstructure units within the TM layers (Figure \$12C). The ex-situ XRD pattern after 20 cycles also





confirms this, as it is almost identical to that after the 1<sup>st</sup> cycle (Figure 4C). More importantly, the superlattice peak is also well retained, indicating the preservation of the Li@Mn<sub>6</sub> superstructure ordering in the TM layers as well as the suppressed Mn migration, which is superior to those reported Mn-rich layered cathodes with the superlattice peaks vanishing after just the 1<sup>st</sup> cycle. <sup>18,49–52</sup> In addition, the LMRO-Ni<sub>0</sub> control after 20 cycles also possesses a similar XRD pattern with the superlattice peak well preserved (Figure S13), specifying again that the Li@Mn<sub>6</sub> superstructure unit is an intrinsic structural property that is unaffected by Ni doping. This is an important proof for the stability of the LMRO structure, which results in the enhanced electrochemical stability.

The cationic and anionic redox behaviors of LMRO during the 1st electrochemical cycle in the voltage range of 2.0-4.8 V were subsequently investigated by the X-ray spectroscopic techniques, including the soft X-ray absorption spectroscopy (XAS), the X-ray photoelectron spectroscopy (XPS), and the Raman spectroscopy. As the ex-situ XAS spectra collected in the total electron yield (TEY) mode shown in Figure \$14A, the pristine LMRO at the open-circuit voltage (OCV) possesses two major Mn  $L_3$ -edge absorption peaks located at  $\sim$ 643.2 and  $\sim$ 640.7 eV and one weak shoulder peak at  $\sim$ 641.7 eV, which indicates the dominance of  $\mathrm{Mn}^{4+}$  and the presence of few Mn<sup>3+</sup>, respectively. 53-55 When charged to 4.5 V and above, the weak shoulder peak disappears, whereas the other strong peaks are maintained, implying the complete oxidation of Mn<sup>3+</sup> to Mn<sup>4+</sup> and further the absence of Mn oxidation beyond the 4+ valence state. The ex-situ Mn 2p XPS spectra confirm the Mn redox since the Mn  $2p_{2/3}$  peak gradually moves to higher binding energy during charge and to lower binding energy during discharge, corresponding to the oxidation of Mn<sup>3+</sup> to Mn<sup>4+</sup> and the reduction of Mn<sup>4+</sup> to Mn<sup>3+</sup>, respectively (Figure S14B). Although Ni also exhibits the similar redox behaviors as Mn, its XPS signal is much weaker due to the low concentration (Figure S14C). This is different from the Li<sub>0.700</sub>[Li<sub>0.222</sub>Mn<sub>0.756</sub>]O<sub>2</sub> cathode, whose 1st-charge compensation is predominantly provided by the redox of O rather than the TMs. 31 With respect to the anionic O redox, the ex-situ O K-edge XAS was firstly employed and collected in the total fluorescence yield (TFY) mode to provide the transitions between the fully occupied O 1s and the empty orbitals above the Fermi level. The O K-edge XAS of the pristine LMRO at the OCV is dominated by two regions, as illustrated in Figure 4D. One is the broad band (>535 eV) involved with the transitions from O 1s to the Mn 4sp and O 2p orbitals (Mn<sub>4sp</sub>-O<sub>2p</sub>), which is composed of two peaks located at  $\sim$ 538 and  $\sim$ 542 eV and derives from the octahedral coordination environment. 41,56 The other is the lower-energy pre-edge region (<535 eV) with a major peak located at  $\sim$ 529.6 eV and a sub-peak at  $\sim$ 532 eV, which corresponds to the transitions from O 1s to the hybridized Mn 3d and O 2p orbitals  $(Mn_{3d}-O_{2p})$  and is the region of most interest. <sup>43,57</sup> Due to the nearly identical preedge O XAS with that at the OCV when charged to 4.5 V, no noticeable change in the O chemical state can be observed, which implies the occurrence of only the Li extraction and very little Mn<sup>3+</sup> oxidation. When the charge voltage is increased to 4.62 and 4.8 V, a small shoulder peak appears at  $\sim$ 531 eV (highlighted by the red arrow in the inset of Figure 4D); this indicates the increase in the density of unoccupied states of O and cannot be attributable to the additional unoccupied states based on Mn because its L-edge XAS and XPS spectra reveal no evidence for further oxidation of the Mn<sup>4+</sup> (Figures S14A and S14B). 41,58 Therefore, these additional unoccupied states should be correlated with the holes primarily in the O 2p orbitals to form the oxidized O<sup>-</sup> species, thus directly demonstrating the high oxidation state of the anionic O<sup>-</sup> formation upon high voltages, which was later proved by the ex-situ O 1s XPS spectra. As shown in Figure S14D, the O 1s XPS peak located at  $\sim$ 529.5 eV is ascribed to the lattice  $O^{2-}$ , and after charging to 4.8 V, a new peak at  $\sim$ 530.3 eV





emerges and is attributed to the oxidized  $O^-$  species, whereas the broad peaks with higher binding energies at  $\sim$ 531.8 and  $\sim$ 533.7 eV are linked to the oxidized deposits and electrolyte decomposition, respectively.

To better visualize the anionic O redox behavior of LMRO during charge to 4.8 V, the powerful in-situ Raman spectroscopy was employed as the probe for the O-related species, especially for the oxidized O-, and the results are displayed in Figure 4E. Prior to charge, the pristine LMRO at the OCV possesses two distinct bands in the Raman spectrum (Figure 4E), namely the typical Eq and A<sub>1q</sub> modes, which are assigned to the  $\delta(O-Mn-O)$  vibrations located at  $\sim$ 480 cm<sup>-1</sup> and the overlapped stretching of the  $v(MnO_6)$  at  $\sim$ 594 cm<sup>-1</sup> with a shoulder peak at  $\sim$ 644 cm<sup>-1</sup>, respectively, <sup>22,43,59,60</sup> whereas another small shoulder peak arises at  $\sim$ 550 cm<sup>-1</sup> that may be derived from the Li@Mn<sub>6</sub> superstructure units.<sup>59</sup> These Raman peaks remain nearly unchanged when charged to ~4.6 V, but then the background of the Raman signals is observed to increase as the charge voltage rises. $^{60}$  Remarkably, a new peak at  $\sim$ 847 cm $^{-1}$  emerges at  $\sim$ 4.64 V within the typical peroxo O<sup>-</sup>-O<sup>-</sup> stretch region (700–900 cm<sup>-1</sup>), which is assigned to the peroxo O-O- bond and further increases during charging to 4.8 V (highlighted by green block in Figure 4E). 41,43,61 This is the direct visualization of the anionic O redox and agrees well with the above results from O K-edge XAS (Figure 4D) and O 1s XPS (Figure S14D). Furthermore, formation of the peroxo O<sup>-</sup>-O<sup>-</sup> bond with a relatively short bond length tends to be along the c-axis (not in the ab plane) because of the decreasing trend in the c-axis length during the high-voltage charge (Figure 4B).62

The gas evolution in the first two cycles (2.0-4.8 V, 0.25C) was then tracked using the in-situ differential electrochemical mass spectrometry (DEMS). Figure 4F shows that an obvious CO<sub>2</sub> peak is detected above 4.5 V in the 1<sup>st</sup> cycle, but only a weak CO<sub>2</sub> signal is observed in the subsequent process. The release of the CO<sub>2</sub> in the early cycles is the product of the decomposition of the carbonates in the electrolyte. Furthermore, despite the observations of the anionic O redox from the spectra of XAS (Figure 4D), XPS (Figure S14D), and Raman (Figure 4E), no apparent O<sub>2</sub> release is recorded during the first two cycles, indicating the high O stability and the limited anionic redox activity in the LMRO cathode. In contrast, stronger and persistent CO<sub>2</sub> and O<sub>2</sub> signals are detected from Li<sub>2</sub>MnO<sub>3</sub> during charging to 4.8 V (Figure S15A), corresponding to the electrolyte decomposition and the lattice O loss, respectively. As for Li<sub>0.7</sub>MnO<sub>2</sub>, a strong CO<sub>2</sub> signal can be observed even at the beginning of charging (Figure S15B). Comparison between the above DEMS measurements verifies that LMRO possesses a more stable structure with fewer side reactions during cycling. In short, these findings from the combined X-ray spectroscopies (XAS and XPS), Raman spectroscopy, and DEMS confirm the stable anionic redox of LMRO upon cycling.

#### Long-term cycling stability

The dQ/dV profiles for the individual  $10^{th}$ ,  $20^{th}$ ,  $50^{th}$ ,  $70^{th}$ , and  $100^{th}$  cycle in the voltage range of 2.0–4.8 V at 0.2C are plotted in Figure 5A to analyze the changes in the electrochemical behavior of the LMRO cathode. The positions of the reduction peaks at  $\sim$ 4.0, 3.2, and 2.9 V and the oxidation peaks at 3.0, 3.8, and 4.5 V remain stable, although the shape of the peaks sharpens, implying the constant electrochemical behavior. The layered phase is well retained in the LMRO cathode after 100 cycles in both the 2.0–4.8 V and 1.5–4.8 V voltage ranges, as shown by the XRD patterns (Figure S16A) and the ample HRTEM images with the clean bulk lattice fringes (Figures S16B–S16F). However, a drop in the superlattice peak intensity after

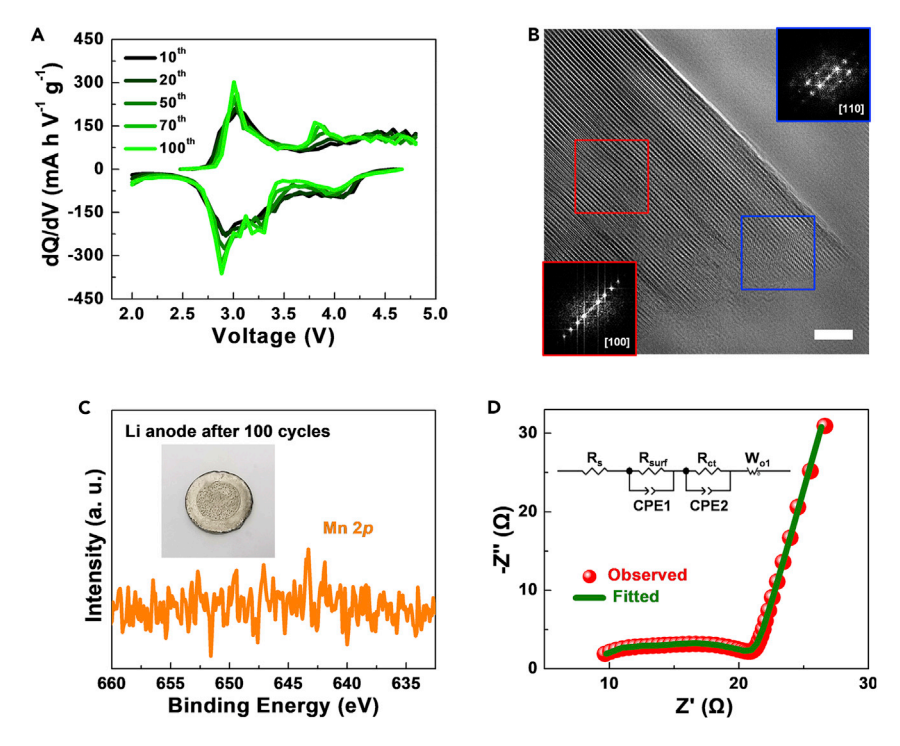


Figure 5. Long-term cycling stability of LMRO

(A) The dQ/dV profiles for the individual  $10^{th}$ ,  $20^{th}$ ,  $50^{th}$ ,  $70^{th}$ , and  $100^{th}$  cycle in the voltage range of 2.0–4.8 V at 0.2C.

(B) HRTEM image after 100 cycles in the voltage range of 2.0-4.8~V at 0.~2C (insets showing the corresponding FFT patterns). Scale bars, 5~nm.

(C) XPS result of Mn 2p after 100 cycles in the voltage range of 2.0–4.8 V at 0. 2C (inset showing the Li anode after 100 cycles).

(D) EIS curve after 100 cycles in the voltage range of  $2.0-4.8\,\mathrm{V}$  at  $0.2\mathrm{C}$  (inset showing the equivalent circuit).

the long-term cycling could indicate the gradual loss of the delocalized Li@Mn<sub>6</sub> superstructure ordering, which may bring instability for both the structure and the electrochemical performance. Meanwhile, similar to the pristine LMRO (Figure 2D), FFT pattern reveals the existence of the minor spinel-like phase on the surface of the bulk layered structure even after 100 cycles (Figure 5B). The Li anode extracted from the coin cells cycled for 100 cycles retains its metallic luster (inset in Figure 5C), and no Mn signal can be detected on its surface using XPS (Figure 5C). In addition, ICP-AES results of the LMRO cathode after 100 cycles also show no change in the Mn/Ni ratio (Table S5), which is consistent with the XPS data and strongly confirms the absence of Mn dissolution. In brief, results from the qualitative and quantitative characterizations after 100 cycles are similar to those from the fresh cathode, demonstrating the excellent structural stability of LMRO during the long-term cycling. Furthermore, the resistance of the LMRO cathode after 100 cycles was investigated using the electrochemical impedance spectroscopy (EIS, Figure 5D) to deconvolute the R<sub>s</sub> from the electrode, electrolyte, and separator, the interfacial resistance R<sub>surf</sub>, and the charge transfer resistance R<sub>ct</sub>. The profile fitting results indicate that the values of R<sub>s</sub>, R<sub>surf</sub>, and  $R_{ct}$  are 8.8, 3.9, and 7.2  $\Omega$ , respectively, which are also far smaller than those of  $Li_2MnO_3$  and  $Li_{0.7}MnO_2$  after 100 cycles (Figure S17). Moreover, after 200 cycles in the voltage range of 2.0-4.8 V at 0.2C, despite the well-maintained bulk layered structure, a transition from the layered to the spinel-like phase as indicated by the lattice fringes and FFT patterns is observed on the LMRO surface due to the





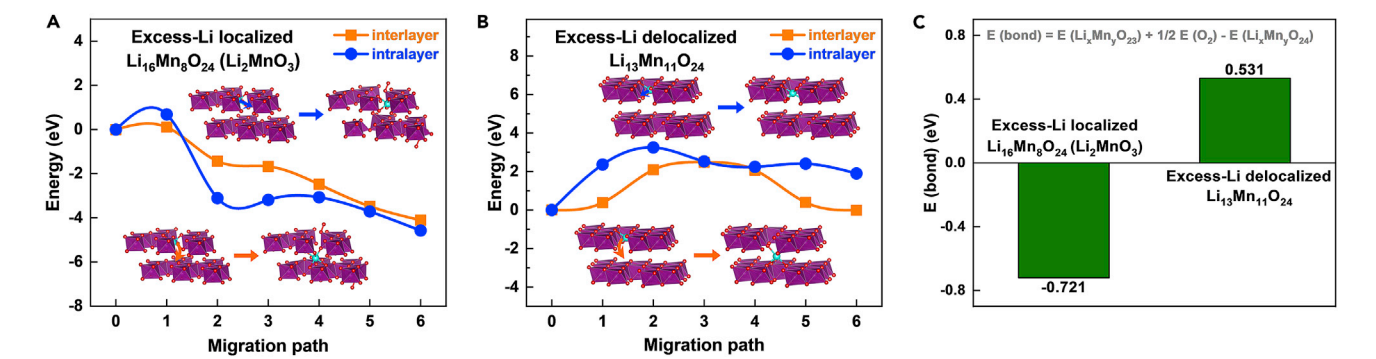


Figure 6. Theoretical study of Li@Mn<sub>6</sub> superstructure units on layered stability

- (A) Mn migration energy of excess-Li localized Li<sub>16</sub>Mn<sub>8</sub>O<sub>24</sub> (Li<sub>2</sub>MnO<sub>3</sub>) after delithiation (inset showing the Mn interlayer and intralayer migration).
- (B) Mn migration energy of excess-Li delocalized  $\text{Li}_{13}\text{Mn}_{11}\text{O}_{24}$  after delithiation (inset showing the Mn interlayer and intralayer migration).
- (C) E(bond) energy of excess-Li localized  $\text{Li}_1 M \text{n}_8 O_{24}$  ( $\text{Li}_2 M \text{n} O_3$ ) and excess-Li delocalized  $\text{Li}_1 M \text{n}_1 O_{24}$  after delithiation.

thickened spinel-like phase region (Figure S18). This is speculated to be induced by the loss of the Li@Mn $_6$  superstructure ordering after 100 cycles (Figure S16A) and the accumulated interfacial side reactions of the electrolyte decomposition at high voltages and is responsible for the gradual decay in the electrochemical performance after  $\sim$ 130 cycles (Figure S7A). Therefore, the combination of the above abundant structural and electrochemical findings strongly indicates that delocalization of the Li@Mn $_6$  superstructure units within the TM layers is indeed a practicable strategy for stabilizing both the structure and electrochemistry of the Li-excess Mn-rich layered cathodes, whose ordering loss will, unfortunately, contribute to the adverse structural transition and further the electrochemical degradation.

#### Theoretical study

To correlate the LMRO's enhanced electrochemical performance with its stable structure, we further carried out theoretical studies to quantitatively investigate the impact of the localized/delocalized Li@Mn6 superstructure units on the Mn migration and O loss of the LMROs (see supplemental information). To begin with, we constructed and optimized a Li<sub>2</sub>MnO<sub>3</sub> supercell (Li<sub>16</sub>Mn<sub>8</sub>O<sub>24</sub>) with the O3-type layered structure and excess-Li localized Li@Mn<sub>6</sub> superstructure units, and then calculated the interlayer and intralayer migration energies for individual Mn after full delithiation. The small energy barriers and down-hill energy sloping presented in Figure 6A clearly indicate that there is little resistance for the interlayer and intralayer Mn migration in the excess-Li localized Li<sub>2</sub>MnO<sub>3</sub> structure, well explaining the origin of the deteriorated structure and electrochemical performance (Figure S11). For comparison, an O3-type supercell (Li<sub>13</sub>Mn<sub>11</sub>O<sub>24</sub>) with excess-Li delocalized Li@Mn<sub>6</sub> superstructure units constructed by replacing 1/12 Mn with Li in the  $LiMnO_2$  structure was also employed and similarly investigated. The calculated energy barriers for its interlayer and intralayer Mn migration are obviously larger, suggesting that the Mn migration is much more difficult in the excess-Li delocalized Mn-rich layered structure (Figure 6B).

The E(bond) energy directly related to the O loss behavior after full delithiation was calculated using the following equation.

$$E(bond) = E(Li_xMn_yO_{23}) + \frac{1}{2}*E(O_2) - E(Li_xMn_yO_{24})$$





The results clearly show that O loss occurs much more easily in the excess-Li localized  $\text{Li}_2\text{MnO}_3$ , whereas rather difficult in the  $\text{Li}_{13}\text{Mn}_{11}\text{O}_{24}$  with excess-Li delocalized  $\text{Li}_2\text{MnO}_3$ , whereas rather difficult in the  $\text{Li}_{13}\text{Mn}_{11}\text{O}_{24}$  with excess-Li delocalized  $\text{Li}_2\text{MnO}_3$ , whereas rather difficult in the Li $_13\text{Mn}_{11}\text{O}_{24}$  with excess-Li delocalized  $\text{Li}_2\text{MnO}_3$  with excess-Li delocalized Li $2\text{MnO}_3$  superstructure and the few Ni dopant does basically not affect the calculation results (Figure S19). These theoretical studies are also capable to match well the extensive structural and electrochemical characterizations elaborated above. Therefore, from theoretical aspects, delocalization of the excess Li and further the  $\text{Li}_2\text{Mn}_3$  superstructure units is indeed an effective approach toward achieving the stable Mn-rich layered cathodes.

#### Origin of the structure stability

As discussed at the beginning, the structure of the Mn-rich layered cathodes needs to be precisely controlled for achieving stable electrochemistry. Although the localized LiMn<sub>6</sub> superstructure units in the TM layers of Li<sub>2</sub>MnO<sub>3</sub> can increase the Mn<sup>3+</sup> valence state to mitigate the J-T distortion in the  $Mn^{(3+)}O_6$  octahedra, unfortunately, they will induce the adverse Mn migration and O loss to occur easily upon deep delitiation, thus causing the severe structural and electrochemical breakdown (Figures 1 and 6). To tackle these challenges, delocalization of the Li@Mn<sub>6</sub> superstructure units within the TM oxide layers is proposed and validated by the LMRO demonstrated herein through massive experimental and theoretical investigations. The LMRO cathode possesses both enhanced structural and electrochemical stabilities, which we attribute to the following key factors: (1) delocalized Li@Mn6 superstructure units in the TM layers can raise the Mn valence from +3 and thus mitigate the structural instability from the J-T distortion to some extent; (2) the intralayer vacancies from the Li extraction upon charge are separated from each other, hindering the Mn migration both into the interlayer and within the intralayer; (3) the O coordination environment is stable with regulated O redox activity to suppress the O loss together with the inhibited Mn migration. Hence, thanks to these effects, the delocalized Li@Mn<sub>6</sub> superstructure units are shown to be the key toward the stable Mnrich layered cathodes.

#### **DISCUSSION**

In this work, we propose a structure modification strategy of delocalization of the Li@Mn $_6$  superstructure units to address the structural instability in Mn-rich layered cathodes and demonstrate its feasibility through a Co-free Mn-rich layered oxide LMRO with delocalized Li@Mn $_6$  superstructure units to enable the layer stability. This cathode delivers a high capacity of 251 mA h g $^{-1}$  (corresponding to 791 W h kg $^{-1}$ ) in the voltage range of 2.0–4.8 V with almost 100% capacity retention even after long-term 100 cycles, which is comparable with the commercial LCO and Ni-rich cathode materials. Detailed experimental and theoretical analyses indicate that the superior electrochemical stability originates from the delocalized Li@Mn $_6$  superstructure units, which suppress the detrimental problems like O loss, Mn dissolution, and further the structure degradation by alleviating the J-T effect and regulating the anionic redox activity. This work introduces a new insight for the comprehensive design and control of the anionic redox activity in the Li-excess Mn-based oxides to achieve both high capacity, energy density, and electrochemical stability for the next-generation cathodes.

#### **EXPERIMENTAL PROCEDURES**

#### Resource availability

Lead contact

Further information and requests for resources and reagents should be directed to and will be fulfilled by the lead contact, Feng Pan (panfeng@pkusz.edu.cn).





#### Materials availability

This study did not generate new unique reagents.

#### Data and code availability

Any additional information required to reanalyze the data reported in this paper is available from the lead contact upon request.

Full experimental procedures, including the material syntheses, characterizations, electrochemical measurements, and theoretical calculations are described in the supplemental information.

#### SUPPLEMENTAL INFORMATION

Supplemental information can be found online at https://doi.org/10.1016/j.chempr. 2022.04.012.

#### **ACKNOWLEDGMENTS**

The authors acknowledge the support from the Shenzhen Science and Technology Research Grant (no. JCYJ20200109140416788) and the Soft Science Research Project of Guangdong Province (no. 2017B030301013).

#### **AUTHOR CONTRIBUTIONS**

Conceptualization, W.H. and C.L.; resources, W.H.; investigation, W.H., J.Q., S.L., Z.C., W.Z., G.R., X.L., and M.Z.; formal analysis, W.H. and C.L.; visualization, W.H. and C.L.; writing – original draft, W.H., C.L., H.C., and F.P.; writing – review & editing, W.H., C.L., and F.P.; funding acquistion, F.P.; supervision, F.P.

#### **DECLARATION OF INTERESTS**

The authors declare no competing interests.

Received: July 16, 2021 Revised: September 18, 2021 Accepted: April 5, 2022 Published: May 6, 2022

#### **REFERENCES**

- Lee, J., Kitchaev, D.A., Kwon, D.H., Lee, C.W., Papp, J.K., Liu, Y.S., Lun, Z., Clément, R.J., Shi, T., McCloskey, B.D., et al. (2018). Reversible Mn<sup>2+</sup>/Mn<sup>4+</sup> double redox in lithium-excess cathode materials. Nature 556, 185–190. https://doi.org/10.1038/s41586-018-0015-4.
- Shi, J.L., Xiao, D.D., Ge, M., Yu, X., Chu, Y., Huang, X., Zhang, X.D., Yin, Y.X., Yang, X.Q., Guo, Y.G., et al. (2018). High-capacity cathode material with high voltage for Li-ion batteries. Adv. Mater. 30, 29333690. https://doi.org/10. 1002/adma.201705575.
- Li, Q.Y., Zhou, D., Zhang, L.J., Ning, D., Chen, Z.H., Xu, Z.J., Gao, R., Liu, X.Z., Xie, D.H., Schumacher, G., and Liu, X.F. (2019). Tuning anionic redox activity and reversibility for a high-capacity Li-rich Mn-based oxide cathode via an integrated strategy. Adv. Funct. Mater. 29, 1806706. https://doi.org/10.1002/adfm. 201806706.
- 4. Li, J., Lin, C., Weng, M., Qiu, Y., Chen, P., Yang, K., Huang, W., Hong, Y., Li, J., Zhang, M., et al.

- (2021). Structural origin of the high-voltage instability of lithium cobalt oxide. Nat. Nanotechnol. 16, 599–605. https://doi.org/10.1038/s41565-021-00855-x.
- Zhang, J.-N., Li, Q.H., Ouyang, C.Y., Yu, X.Q., Ge, M.Y., Huang, X.J., Hu, E.Y., Ma, C., Li, S.F., Xiao, R.J., et al. (2019). Trace doping of multiple elements enables stable battery cycling of LiCoO<sub>2</sub> at 4.6 V. Nat. Energy 4, 594–603. https://doi.org/10.1038/s41560-019-0409-z.
- Li, W.D., Liu, X.M., Celio, H.G., Smith, P., Dolocan, A., Chi, M.F., and Manthiram, A. (2018). Mn versus Al in layered oxide cathodes in lithium-ion batteries: a comprehensive evaluation on long-term cyclability. Adv. Energy Mater. 8, 1703154. https://doi.org/10. 1002/aenm.201703154.
- Xu, C., Märker, K., Lee, J., Mahadevegowda, A., Reeves, P.J., Day, S.J., Groh, M.F., Emge, S.P., Ducati, C., Layla Mehdi, B., et al. (2021). Bulk fatigue induced by surface reconstruction in

- layered Ni-rich cathodes for Li-ion batteries. Nat. Mater. 20, 84–92. https://doi.org/10.1038/s41563-020-0767-8.
- Bi, Y.J., Tao, J.H., Wu, Y.Q., Li, L.Z., Xu, Y.B., Hu, E.Y., Wu, B.B., Hu, J.T., Wang, C.M., Zhang, J.-G., et al. (2020). Reversible planar gliding and microcracking in a single-crystalline Ni-rich cathode. Science 370, 1313–1317. https://doi. org/10.1126/science.abc3167.
- Choi, J.U., Voronina, N., Sun, Y.K., and Myung, S.T. (2020). Recent progress and perspective of advanced high-energy Co-less Ni-rich cathodes for Li-ion batteries: yesterday, today, and tomorrow. Adv. Energy Mater. 10, 2002027. https://doi.org/10.1002/aenm. 202002027.
- Kim, U.-H., Park, G.-T., Son, B.-K., Nam, G.W., Liu, J., Kuo, L.-Y., Kaghazchi, P., Yoon, C.S., and Sun, Y.-K. (2020). Heuristic solution for achieving long-term cycle stability for Ni-rich layered cathodes at full depth of discharge.





- Nat. Energy 5, 860–869. https://doi.org/10.1038/s41560-020-00693-6.
- Huang, W., Lin, C., Zhang, M., Li, S., Chen, Z., Zhao, W., Zhu, C., Zhao, Q., Chen, H., and Pan, F. (2021). Revealing roles of Co and Ni in Mnrich layered cathodes. Adv. Energy Mater. 11, 2102646. https://doi.org/10.1002/aenm. 202102646.
- Ammundsen, B., and Paulsen, J. (2001). Novel lithium-ion cathode materials based on layered manganese oxides. Adv. Mater. 13, 943–956. https://doi.org/10.1002/1521-4095(200107) 13:12/13<-943::AID-ADMA943>3.0.CO;2-J.
- Hwang, S.-J., Park, H.-S., Choy, J.-H., and Campet, G. (2000). Evolution of local structure around manganese in layered LiMnO<sub>2</sub> upon chemical and electrochemical delithiation/relithiation. Chem. Mater. 12, 1818–1826. https:// doi.org/10.1021/cm9905491.
- Tian, M., Gao, Y., Wang, Z., and Chen, L. (2016). Understanding structural stability of monoclinic LiMnO<sub>2</sub> and NaMnO<sub>2</sub> upon deintercalation. Phys. Chem. Chem. Phys. 18, 17345–17350. https://doi.org/10.1039/ C6CP02019D.
- Armstrong, A.R., and Bruce, P.G. (1996).
  Synthesis of layered LiMnO<sub>2</sub> as an electrode for rechargeable lithium batteries. Nature 381, 499–500. https://doi.org/10.1038/381499a0.
- Wang, R., He, X., He, L., Wang, F., Xiao, R., Gu, L., Li, H., and Chen, L. (2013). Atomic structure of Li<sub>2</sub>MnO<sub>3</sub> after partical delithiation. Adv. Energy Mater. 3, 1358–1367. https://doi.org/ 10.1002/aenm.201200842.
- Rana, J., Papp, J.K., Lebens-Higgins, Z., Zuba, M., Kaufman, L.A., Goel, A., Schmuch, R., Winter, M., Whittingham, M.S., Yang, W., et al. (2020). Quantifying the capacity contributions during activation of Li<sub>2</sub>MnO<sub>3</sub>. ACS Energy Lett. 5, 634–641. https://doi.org/10.1021/acsenergylett.9b02799.
- House, R.A., Rees, G.J., Pérez-Osorio, M.A., Marie, J.-J., Boivin, E., Robertson, A.W., Nag, A., Garcia-Fernandez, M., Zhou, K.-J., and Bruce, P.G. (2020). First-cycle voltage hysteresis in Li-rich 3d cathodes associated with molecular O<sub>2</sub> trapped in the bulk. Nat. Energy 5, 777–785. https://doi.org/10.1038/s41560-020-00697-2.
- Kim, S., Cho, W., Zhang, X., Oshima, Y., and Choi, J.W. (2016). A stable lithium-rich surface structure for lithium-rich layered cathode materials. Nat. Commun. 7, 13598. https://doi. org/10.1038/ncomms13598.
- Redel, K., Kulka, A., Plewa, A., and Molenda, J. (2019). High-performance Li-rich layered transition metal oxide cathode materials for Liion batteries. J. Electrochem. Soc. 166, A5333– A5342. https://doi.org/10.1149/2.0511903jes.
- Phillips, P.J., Bareño, J., Li, Y., Abraham, D.P., and Klie, R.F. (2015). On the localized nature of the structural transformations of Li<sub>2</sub>MnO<sub>3</sub> following electrochemical cycling. Adv. Energy Mater. 5, 1501252. https://doi.org/10.1002/ aenm.201501252.
- Li, X., Qiao, Y., Guo, S., Xu, Z., Zhu, H., Zhang, X., Yuan, Y., He, P., Ishida, M., and Zhou, H. (2018). Direct visualization of the reversible O<sup>2-</sup>/O<sup>-</sup> redox process in Li-rich cathode

- materials. Adv. Mater. 30, e1705197. https://doi.org/10.1002/adma.201705197.
- Liu, Y., Zhu, H., Zhu, H., Ren, Y., Zhu, Y., Huang, Y., Dai, L., Dou, S., Xu, J., Sun, C.-J., et al. (2021). Modulating the surface ligand orientation for stabilized anionic redox in Li-rich oxide cathodes. Adv. Energy Mater. 11, 2003479. https://doi.org/10.1002/aenm.202003479.
- 24. Li, F., Wang, Y.Y., Gao, S.L., Hou, P.Y., and Zhang, L.Q. (2017). Mitigating the capacity and voltage decay of lithium-rich layered oxide cathodes by fabricating Ni/Mn graded surface. J. Mater. Chem. A 5, 24758–24766. https://doi.org/10.1039/C7TA07659B.
- Wang, J., He, X., Paillard, E., Laszczynski, N., Li, J., and Passerini, S. (2016). Lithium- and manganese-rich oxide cathode materials for high-energy lithium ion batteries. Adv. Energy Mater. 6, 1600906. https://doi.org/10.1002/ aenm.201600906.
- Xu, J., Sun, M., Qiao, R., Renfrew, S.E., Ma, L., Wu, T., Hwang, S., Nordlund, D., Su, D., Amine, K., et al. (2018). Elucidating anionic oxygen activity in lithium-rich layered oxides. Nat. Commun. 9, 947. https://doi.org/10.1038/ s41467-018-03403-9.
- Zhao, S., Yan, K., Zhang, J., Sun, B., and Wang, G. (2021). Reaction mechanisms of layered lithium-rich cathode materials for high-energy lithium-ion batteries. Angew. Chem. Int. Ed. Engl. 60, 2208–2220. https://doi.org/10.1002/ apic.202000262
- Seo, D.-H., Lee, J., Urban, A., Malik, R., Kang, S., and Ceder, G. (2016). The structural and chemical origin of the oxygen redox activity in layered and cation-disordered Li-excess cathode materials. Nat. Chem. 8, 692–697. https://doi.org/10.1038/nchem.2524.
- Gu, M., Belharouak, I., Zheng, J.M., Wu, H.M., Xiao, J., Genc, A., Amine, K., Thevuthasan, S., Baer, D.R., Zhang, J.-G., et al. (2013). Formation of the spinel phase in the layered composite cathode used in Li-ion batteries. ACS Nano 7, 760–767. https://doi.org/10.1021/nn305065u.
- Lee, E., and Persson, K.A. (2014). Structural and chemical evolution of the layered Li-excess Li<sub>x</sub>MnO<sub>3</sub> as a function of Li content from firstprinciples calculations. Adv. Energy Mater. 4, 1400498. https://doi.org/10.1002/aenm. 201400498.
- Song, J., Li, B., Chen, Y.Y., Zuo, Y.X., Ning, F.H., Shang, H.F., Feng, G., Liu, N., Shen, C.H., Ai, X.P., and Xia, D. (2020). A high-performance Li– Mn–O Li-rich cathode material with rhombohedral symmetry via intralayer Li/Mn disordering. Adv. Mater. 32, e2000190. https:// doi.org/10.1002/adma.202000190.
- Eum, D.G., Kim, B., Kim, S.J., Park, H., Wu, J.P., Cho, S.P., Yoon, G., Lee, M.H., Jung, S.K., Yang, W.L., et al. (2020). Voltage decay and redox asymmetry mitigation by reversible cation migration in lithium-rich layered oxide electrodes. Nat. Mater. 19, 419–427. https:// doi.org/10.1038/s41563-019-0572-4.
- De Boisse, B.M., Jang, J., Okubo, M., and Yamada, A. (2018). Cobalt-free O2-type lithium-rich layered oxides. J. Electrochem. Soc. 165, A3630–A3633. https://doi.org/10. 1149/2.1331814jes.

- Mohanty, D., Li, J.L., Abraham, D.P., Huq, A., Payzant, E.A., Wood, D.L., and Daniel, C. (2014). Unraveling the voltage-fade mechanism in high-energy-density lithium-ion batteries: origin of the tetrahedral cations for spinel conversion. Chem. Mater. 26, 6272–6280. https://doi.org/10.1021/cm5031415.
- Yan, P., Nie, A., Zheng, J., Zhou, Y., Lu, D., Zhang, X., Xu, R., Belharouak, I., Zu, X., Xiao, J., et al. (2015). Evolution of lattice structure and chemical composition of the surface reconstruction layer in Li<sub>1.2</sub>Ni<sub>0.2</sub>Mn<sub>0.6</sub>O<sub>2</sub> cathode material for lithium ion batteries. Nano Lett. 15, 514–522. https://doi.org/10.1021/ nl5038598
- Myeong, S., Cho, W., Jin, W., Hwang, J., Yoon, M., Yoo, Y., Nam, G., Jang, H., Han, J.G., Choi, N.S., et al. (2018). Understanding voltage decay in lithium-excess layered cathode materials through oxygen-centred structural arrangement. Nat. Commun. 9, 3285. https:// doi.org/10.1038/s41467-018-05802-4.
- 37. Hwang, J., Myeong, S., Jin, W., Jang, H., Nam, G., Yoon, M., Kim, S.H., Joo, S.H., Kwak, S.K., Kim, M.G., and Cho, J. (2020). Excess-Li localization triggers chemical irreversibility in Li- and Mn-rich layered oxides. Adv. Mater. 32, e2001944. https://doi.org/10.1002/adma. 202001944.
- Hwang, J., Myeong, S., Lee, E., Jang, H., Yoon, M., Cha, H., Sung, J., Kim, M.G., Seo, D.-H., and Cho, J. (2021). Lattice-oxygen-stabilized Li- and Mn-rich cathodes with sub-micrometer particles by modifying the excess-Li distribution. Adv. Mater. 33, e2100352. https:// doi.org/10.1002/adma.202100352.
- Sun, G., Yu, F.-D., Que, L.-F., Deng, L., Wang, M.-J., Jiang, Y.-S., Shao, G.J., and Wang, Z.-B. (2019). Local electronic structure modulation enhances operating voltage in Li-rich cathodes. Nano Energy 66, 104102. https://doi. org/10.1016/j.nanoen.2019.104102.
- Sun, G., Yu, F.D., Zhao, C.T., Yu, R.Z., Farnum, S., Shao, G.J., Sun, X.L., and Wang, Z.B. (2021). Decoupling the voltage hysteresis of Li-rich cathodes: electrochemical monitoring, modulation anionic redox chemistry and theoretical verifying. Adv. Funct. Mater. 31, 2002643. https://doi.org/10.1002/adfm. 202002643.
- Luo, K., Roberts, M.R., Hao, R., Guerrini, N., Pickup, D.M., Liu, Y.-S., Edström, K., Guo, J., Chadwick, A.V., Duda, L.C., and Bruce, P.G. (2016). Charge-compensation in 3d-transitionmetal-oxide intercalation cathodes through the generation of localized electron holes on oxygen. Nat. Chem. 8, 684–691. https://doi. org/10.1038/nchem.2471.
- Assat, G., Foix, D., Delacourt, C., Iadecola, A., Dedryvère, R., and Tarascon, J.-M. (2017). Fundamental interplay between anionic/ cationic redox governing the kinetics and thermodynamics of lithium-rich cathodes. Nat. Commun. 8, 2219. https://doi.org/10.1038/ s41467-017-02291-9
- Cao, X., Li, H.F., Qiao, Y., Jia, M., Li, X., Cabana, J., and Zhou, H.S. (2020). Stabilizing anionic redox chemistry in a Mn-based layered oxide cathode constructed by Li-deficient pristine state. Adv. Mater. 33, 2004280. https://doi.org/ 10.1002/adma.202004280.





- 44. Lyu, Y.C., Hu, E.Y., Xiao, D.D., Wang, Y., Yu, X.Q., Xu, G.L., Ehrlich, S.N., Amine, K., Gu, L., Yang, X.-Q., and Li, H. (2017). Correlations between transition-metal chemistry, local structure, and global structure in Li<sub>2</sub>Ru<sub>0.5</sub>Mn<sub>0.5</sub>O<sub>3</sub> investigated in a wide voltage window. Chem. Mater. 29, 9053–9065. https://doi.org/10.1021/acs.chemmater.7b02299.
- 45. Zheng, S.Y., Zheng, F., Liu, H.D., Zhong, G.M., Wu, J., Feng, M., Wu, Q.H., Zuo, W.H., Hong, C.Y., Chen, Y., et al. (2019). Novel ordered rocksalt-type lithium-rich  $\text{Li}_2\text{Ru}_{1-x}\text{Ni}_x\text{O}_{3-\delta}$  (0.3  $\leq$  x  $\leq$  0.5) cathode material with tunable anionic redox potential. ACS Appl. Energy Mater. 2, 5933–5944. https://doi.org/10.1021/acsaem.9b01051.
- Li, Q., Li, G., Fu, C., Luo, D., Fan, J., Xie, D., and Li, L. (2015). Balancing stability and specific energy in Li-rich cathodes for lithium ion batteries: a case study of a novel Li-Mn-ni-Co oxide. J. Mater. Chem. A 3, 10592–10602. https://doi.org/10.1039/C5TA00929D.
- Lee, M.-J., Lho, E., Oh, P., Son, Y., and Cho, J. (2017). Simultaneous surface modification method for 0.4Li<sub>2</sub>MnO<sub>3</sub> 0.6LiNi<sub>1/3</sub>Co<sub>1/3</sub>Mn<sub>1/3</sub>O<sub>2</sub> cathode material for lithium ion batteries: acid treatment and LiCoPO<sub>4</sub> coating. Nano Res. 10, 4210–4220. https://doi.org/10.1007/s12274-017-1662-8.
- Hu, S.J., Li, Y., Chen, Y.H., Peng, J.M., Zhou, T.F., Pang, W.K., Didier, C., Peterson, V.K., Wang, H.Q., Li, Q.Y., and Guo, Z.P. (2019). Insight of a phase compatible surface coating for long-durable Li-rich layered oxide cathode. Adv. Energy Mater. 9, 1901795. https://doi.org/ 10.1002/aenm.201901795.
- Sun, J., Sheng, C., Cao, X., Wang, P., He, P., Yang, H., Chang, Z., Yue, X., and Zhou, H. (2021). Restraining oxygen release and suppressing structure distortion in singlecrystal Li-rich layered cathode materials. Adv. Funct. Mater. 35, 2110295. https://doi.org/10. 1002/adfm 202110295
- 50. Yang, Z., Zhong, J., Feng, J., Li, J., and Kang, F. (2021). Highly reversible anion redox of

- manganese-based cathode material realized by electrochemical ion exchange for lithiumion batteries. Adv. Funct. Mater. 31, 2103594. https://doi.org/10.1002/adfm.202103594.
- Wen, X., Yin, C., Qiu, B., Wan, L., Zhou, Y., Wei, Z., Shi, Z., Huang, X., Gu, Q., and Liu, Z. (2022). Controls of oxygen-partial pressure to accelerate the electrochemical activation in Co-free Li-rich layered oxide cathodes. J. Power Sources 523, 231022. https://doi.org/ 10.1016/j.jpowsour.2022.231022.
- Yabuuchi, N., Yoshii, K., Myung, S.-T., Nakai, I., and Komaba, S. (2011). Detailed studies of a high-capacity electrode material for rechargeable batteres, Li2MnO3-LiCo<sub>1/3</sub>Ni<sub>1/3</sub>Mn<sub>1/3</sub>O<sub>2</sub>. J. Am. Chem. Soc. 133, 4404–4419. https://doi.org/10.1021/ja108588y.
- 53. Lin, F., Markus, I.M., Nordlund, D., Weng, T.-C., Asta, M.D., Xin, H.L., and Doeff, M.M. (2014). Surface reconstruction and chemical evolution of stoichiometric layered cathode materials for lithium-ion batteries. Nat. Commun. 5, 3529. https://doi.org/10.1038/ncomms4529.
- 54. Zhang, J.C., Zhang, Q.H., Wong, D., Zhang, N., Ren, G.X., Gu, L., Schulz, C., He, L.H., Yu, Y., and Liu, X.F. (2021). Addressing voltage decay in Li-rich cathodes by broadening the gap between metallic and anionic bands. Nat. Commun. 12, 3071. https://doi.org/10.1038/ s41467-021-23365-9.
- 55. Oishi, M., Yamanaka, K., Watanabe, I., Shimoda, K., Matsunaga, T., Arai, H., Ukyo, Y., Uchimoto, Y., Ogumi, Z., and Ohta, T. (2016). Direct observation of reversible oxygen anion redox reaction in Li-rich manganese oxide, Li<sub>2</sub>MnO<sub>3</sub>, studied by soft X-ray absorption spectroscopy. J. Mater. Chem. A 4, 9293–9302. https://doi.org/10.1039/C6TA00174B.
- De Groot, F.M.F., Grioni, M., Fuggle, J.C., Ghijsen, J., Sawatzky, G.A., and Petersen, H. (1989). Oxygen 1s x-ray-absorption edges of transition-metal oxides. Phys. Rev. B Condens. Matter 40, 5715–5723. https://doi.org/10.1103/ PhysRevB.40.5715.

- Oishi, M., Yogi, C., Watanabe, I., Ohta, T., Orikasa, Y., Uchimoto, Y., and Ogumi, Z. (2015). Direct observation of reversible charge compensation by oxygen ion in Li-rich manganese layered oxide positive electrode material, Li<sub>1.16</sub>Ni<sub>0.15</sub>Co<sub>0.19</sub>Mn<sub>0.50</sub>O<sub>2</sub>. J. Power Sources 276, 89–94. https://doi.org/10.1016/j. jpowsour.2014.11.104.
- Koga, H., Croguennec, L., Ménétrier, M., Mannessiez, P., Weill, F., Delmas, C., and Belin, S. (2014). Operando X-ray absorption study of the redox processes involved upon cycling of the Li-rich layered oxide Li<sub>1.20</sub>Mn<sub>0.54</sub>Co<sub>0.13</sub>Ni<sub>0.13</sub>O<sub>2</sub> in Li ion batteries. J. Phys. Chem. C *118*, 5700–5709. https://doi. org/10.1021/jp412197z.
- 59. Lanz, P., Villevieille, C., and Novák, P. (2014). Ex situ and in situ Raman microscopic investigation of the differences between stoichiometric LiMO<sub>2</sub> and highenergy xLi<sub>2</sub>MnO<sub>3</sub>·(1–x)LiMO<sub>2</sub> (M = Ni, Co, Mn). Electrochim. Acta 130, 206–212. https://doi.org/10.1016/j.electacta.2014. 03.004.
- Venkateswara Rao, C.V., Soler, J., Katiyar, R., Shojan, J., West, W.C., and Katiyar, R.S. (2014). Investigations on electrochemical behavior and structural stability of Li<sub>1.2</sub>Mn<sub>0.54</sub>Ni<sub>0.13</sub>Co<sub>0.13</sub>O<sub>2</sub> lithium-ion cathodes via *in-situ* and *ex-situ* Raman spectroscopy. J. Phys. Chem. C *118*, 14133–14141. https://doi.org/10.1021/ jp501777v.
- 61. Yu, Q., and Ye, S. (2015). In situ study of oxygen reduction in dimethyl sulfoxide (DMSO) solution: a fundamental study for development of the lithium–oxygen battery. J. Phys. Chem. C 119, 12236–12250. https://doi.org/10.1021/acs.ipcc.5b03370.
- 62. Saubanère, M., McCalla, E., Tarascon, J.-M., and Doublet, M.-L. (2016). The intriguing question of anionic redox in high-energy density cathodes for Li-ion batteries. Energy Environ. Sci. 9, 984–991. https://doi.org/10. 1039/C5EE03048J.